A Reduced Order Model based on Artificial Neural Networks for nonlinear aeroelastic phenomena and application to composite material beams

A.J. Torregrosa, A. Gil, P. Quintero, A. Cremades *

CMT-Motores Térmicos, Universitat Politècnica de València, Camino de Vera s/n, Valencia, 46022, Spain

ARTICLE INFO

ABSTRACT

Applications of composite materials in industry have increased due to their high stiffness-to-weight ratio. In the particular case of unidirectional fibers or perpendicular fabrics, the materials behavior is orthotropic, so that an extra degree of freedom, related to the orientation of the fibers, must be included in the structural optimization. Composite material thin walled beam models have been developed for reducing the computational cost of the simulations. Traditionally, these models have been coupled with potential aerodynamics to calculate the aeroelastic response, and thus, the viscous nonlinear effects have been omitted. In order to capture these effects, this manuscript focus on the development of a Reduced Order Model enhanced by an Artificial Neural Network for the analysis of composite structures under aerodynamic loads. The presented methodology shows the training process of the neural network, the comparison with high fidelity simulations and the design optimization of a carbon fiber laminated foam beam. It is demonstrated that the model reduces the computational cost by orders of magnitude, while still capturing structural couplings and being capable of increasing the flutter velocity by more than 10% with respect to the longitudinal orientation.

1. Introduction

Due to their high stiffness-to-weight ratio, the importance of composite materials has grown significantly in the last decades. An ample research has been carried out on composite laminates, promoted by the diversity and severity of the loads that light structures must meet in the aerospace [1], automotive [2], naval [3], energy [4,5] or civil [6,7] industries. For instance, in the aerospace industry, the European objectives for 2050 [8] require a substantial decrease in the frame weight. As a possible solution, the use of fiber-reinforced polymers has been proposed in numerous research works, such as those reported by Khalil [9] and Rajpal et al. [10].

In addition, the use of composite materials allows developing designs that improve the dynamic behavior of the whole structure. In the work of Attaran et al. [11] the possibility of improving the aeroelastic limits of the structure as a result of the bend–twist coupling generated by the fiber orientation, as demonstrated by Chadra et al. [12], was analyzed numerically and experimentally. Other authors such as Geroghiades and Banerjee [13] analytically studied similar effects. In fact, two different structural coupling effects can be observed in orthotropic materials [14]: wash-in, or positive bend–twist coupling (augmentation of the flight loads), and wash-out, or negative bend–twist coupling (alleviation of the flight loads).

Different tools and methodologies have been proposed in order to model and calculate composite thin walled structures. Many authors have used finite element analysis (FEA) to obtain the internal stress and strain of the composite elements [15]. When the loads are applied by a flow, the Fluid Structure Interaction (FSI) problem can be solved by means of a coupled Computational Solid Dynamics (CSD)/Computational Fluid Dynamics (CFD) simulation [16,17]. However, the fully coupled simulation of an elastic solid and a viscous flow is not affordable at the initial stages of the design process [18].

The reduction of the associated computational cost has traditionally been achieved by reducing the dimensions of the problem. The classic reference of Dowell [19] proposes an equivalent section for representing a whole isotropic beam. This equivalent section was adopted in many works such as that reported by Baxevanou et al. [20], who simulated classical flutter in wind turbine rigid airfoils coupled with torsional and linear springs. However, the concept of an equivalent section is limited, as the boundary conditions may be changed and the effect of secondary modes is not straightforwardly reproduced. In order to overcome these limitations, on one hand Gil et al. [21] proposed a methodology for obtaining the 2D equivalent section of an arbitrary beam. Nevertheless, the use of their model was limited to isotropic or slightly orthotropic structures. On the other hand, a wide amount of

---

Symbols

α	Angle of attack
$\bar{\alpha}$	Mean angle of attack
α_0	Initial incidence of the airflow
$\Delta\alpha$	Amplitude of the angle of attack respect to the mean
Δt	Time step
Δt_i	Internal time step
ϵ	Error
θ	Rotation around z axis
$\bar{\theta}$	Mean rotation around z axis
θ_0	Initial incidence of the beam
θ_f	Orientation of the laminate ply
θ_{max}	Maximum twist of the beam
v	Poisson's ratio
v_{lt}	Longitudinal–transverse Poisson's ratio of the laminate ply
v_{tt}	Transverse- transverse Poisson's ratio of the laminate ply
ρ	Density of the material
ρ_∞	Density of the air
c	Chord of the beam
C_L	3D lift coefficient
c_l	2D lift coefficient
c_l^{st}	Steady 2D lift coefficient
c_l^{dyn}	Dynamic 2D lift coefficient
C_M	3D moment coefficient
c_m	2D moment coefficient
c_m^{st}	Steady 2D moment coefficient
c_m^{dyn}	Dynamic 2D moment coefficient
c_p	Power coefficient
E	Elastic modulus
E^*	Nondimensional stiffness
E_l	Longitudinal elastic modulus of the laminate ply
E_t	Transverse elastic modulus of the laminate ply
$\vec{F}$	Load vector
G	Shear modulus
G_{lt}	Longitudinal–transverse shear modulus of the laminate ply
G_{tt}	Transverse–transverse shear modulus of the laminate ply
h	Thickness of the beam
h_{ply}	Thickness of the laminate ply
$\mathbf{K}$	Stiffness matrix
L	Length of the beam
$\mathbf{M}$	Mass matrix
T	Period
tol	Maximum error admitted
t	Time

t^*	Nondimensional time
t_{max}	Total simulation time
V_∞	Free stream velocity
$\vec{u}$	Deformation vector
v	Vertical deformation
v_0	Initial vertical displacement
$\bar{v}$	Mean vertical deformation
z	Longitudinal coordinate

warping of an anisotropic open section using the Timoshenko model for transverse shear and the Vlasov model for nonuniform torsion, and Farsadi et al. [25] applied the Librescu composite thin walled beam (TWB) theory [26] to the optimization of the aeroelastic response of a wing. Even though multiple structural models for thin walled beams were considered in the previous research, they were still uncoupled with any nonlinear viscous aerodynamic model.

Relative to the aerodynamic loads, simulating Navier–Stokes equations for the aeroelastic motion of an equivalent rigid section requires high computational resources for both the initial design and the structural optimization. For this reason, many authors have proposed Reduced Order Models (ROMs), some of which are based on Proper Orthogonal Decomposition (POD) [27–29]. However, citing the words of Li et al. [30]: "POD ROMs are only suitable for a frozen aeroelastic model configuration". Other researchers have developed aeroelastic models based on Artificial Neural networks (ANN) [31]. Wu and Kareem [32] divided the aerodynamic coefficient into a static and a dynamic term to model the hysteretic nonlinear behavior of bridge decks. Another example is the research of Chen et al. [33], in which the authors used experimental data to feed the neural network. Moreover, in the works of Abbas et al. [34] and Li et al. [35] the artificial neural network is trained using results from CFD simulations. Finally, Torregrosa et al. [36] evaluated the application of feed-forward (FNN) and long short-term memory (LSTM) neurons, evidencing that FNN can reduce computational cost when compared to LSTM without accuracy penalties. Nevertheless, the previous ANN enhanced models only focus on the transient aerodynamics or couple the surrogate models with spring–mass models. They do not take into account the structural behavior of orthotropic material thin walled cross-section beams.

This article aims to extend the research found in the literature by adding an Artificial Neural Network to the Reduced Order Models for orthotropic thin walled beams (TWB). The objective of adding the Neural Network is to calculate nonlinear complex aerodynamics, including viscous effects to the simulations. The structural model is based on the Librescu composite TWB theory [37], and derives the equivalent structure applying classical lamination theory. This beam model is validated against the literature [38–40] and then coupled with an aerodynamic surrogate model based on Feed-forward neural networks (FFN), which was developed and tested in [36]. The results of the ROM are compared with CSD/CFD simulations in order to validate the procedure and solvers. It is demonstrated that the model allows reducing the computational cost, while predicting nonlinear aerodynamic effects and calculating structural couplings of the orthotropic material.

The paper is organized as follows: firstly, in Section 2, the methodology is explained, showing the case studied, the ROM structure and the CSD/CFD configuration; then, in Section 3 the main results of the research are shown; the ROM is compared with high accuracy simulations and the influence of the fiber orientation in the test case is discussed. Finally, the main conclusions are commented in Section 4.

research can be found in the literature where the three dimensional structure is simplified to a one dimensional beam. In Ghafari and Rezaeepazhand [22], the cross-section mass and stiffness properties were studied and then applied to a beam model for the whole beam simulation.

Beam models have been widely used to model orthotropic material structures. For instance, Carrera et al. [23] applied the Carrera Unified Formulation (CUF) to obtain the vibrational state of a rotating blade; Dhadwal and Jung [24] calculated the shear and torsional
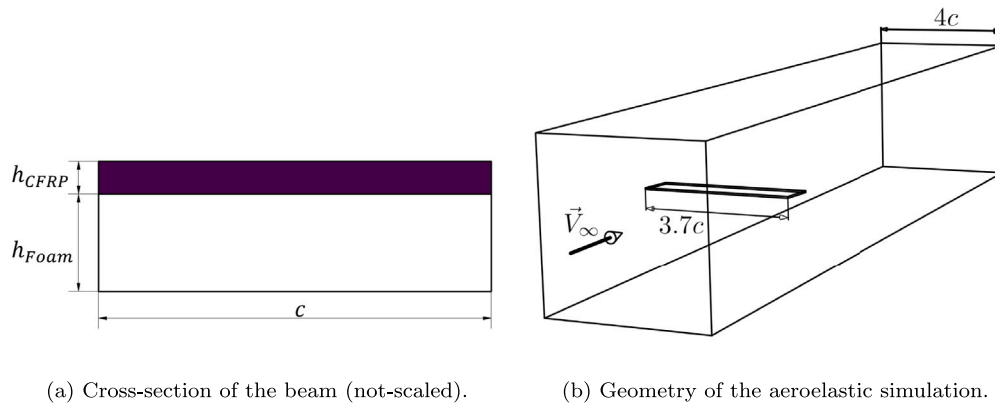
(a) Cross-section of the beam (not-scaled).

(b) Geometry of the aeroelastic simulation.

Fig. 1. Geometry of beam and wind tunnel domain.

Table 1
Material properties of CFRP and foam, based on the works of Qin and Librescu [41] and Koohi et al. [42] respectively. E_l and E_t are the longitudinal and transverse elastic modulus respectively, G_{lt} and G_{tt} the longitudinal–transverse and transverse–transverse shear modulus, v_{lt} and v_{tt} the longitudinal–transverse and transverse–transverse Poisson ratios, h_{ply} is the ply thickness and ρ is the material density.

	AS4/3501–6	Foam		AS4/3501–6	Foam
E_l (MPa)	141960	15	v_{lt} (-)	0.42	0.28
E_t (MPa)	9780	15	v_{tt} (-)	0.50	0.28
G_{lt} (MPa)	6000	8	h_{ply} (mm)	0.13	3.87
G_{tt} (MPa)	4830	8	ρ (kg/m^3)	1445	35

2. Material and methods

In this section, the methodology used in the article is presented. The geometry, boundary conditions and the material are defined. Then, the two different approaches procedures are included. For the CSD/CFD simulation, the models are discussed and the mesh is shown. Finally, the algorithm and models of the ROM are presented and explained.

2.1. Case of study

Along this work, a carbon fiber laminated foam squared-section beam is used. This geometry was previously used in Gil et al. [21] and Torregrosa et al. [36]. The beam had a length of $L = 370$ mm, a chord of $c = 100$ mm and its thickness was $h = 4$ mm. The laminate of the studied geometry presents a $[\theta_f/-]$ configuration where θ_f is the orientation of the fiber, which is varied from −90 to 90 deg. The thickness of the carbon-fiber-reinforced polymer (CFRP) ply is 0.13 mm and the foam ply completes the total thickness of the laminate. The geometry of the cross-section is presented in Fig. 1(a). Note that the origin of the coordinate system is located at the center of the root cross-section. The beam geometry is clamped by one end and the free faces are connected to the fluid. The beam is simulated inside a square cross-section wind channel. The width of the tunnel is equal to $4c$. The walls of the tunnel have been defined as slipping [43], while the boundaries upwash and downwash have been defined as velocity inlet and pressure outlet respectively. These boundaries have been placed far enough for not affecting the results, $5c$ upwash and $15c$ downwash. Different airflow velocities are simulated to obtain aeroelastic deformations along the working range, containing the Reynolds number in the range $6 \cdot 10^3$–$50 \cdot 10^3$. The aerodynamic loads are applied to the beam surface. Fig. 1(b) shows the domain of the aeroelastic simulation.

2.2. CSD/CFD methodology

The aeroelastic ROM was compared with a CSD/CFD simulation for geometry of Section 2.1. The conservation equations were solved for the solid and the fluid by using the commercial software Simcenter STAR-CCM+®, and a setup similar to that used by Gil et al. [21]. The displacements of the structure due to the applied loads were solved by means of a Finite Element Method (FEM), the fluid flow was solved using the Finite Volume Method (FVM) to discretize the conservation equations applied to a fluid, and these two simulations were coupled through a mapped contact interface. This interface was located between the solid and the fluid, generating an indirect association between the faces and allowing a non-conformal mesh. In order to define the material, each ply of the layup was meshed independently and then connected thought a contact interface.

The equations were calculated on a polyhedral mesh, as presented in Fig. 2. A final mesh of $5.29 \cdot 10^6$ elements for the fluid and $1.60 \cdot 10^5$ for the solid was selected following a mesh independence analysis with a maximum error of 2% in the main forces and moments.

2.3. Aeroelastic ROM

The aeroelastic ROM is presented in Fig. 3. The structure of the model may be divided into three main blocks or submodels: initialization, load estimation and coupled solver.

In the initialization block, the initial and boundary conditions are set and the material of the beam is selected. In addition, the mechanical properties of the generic cross-section of the beam are calculated using the Librescu and Song [37] theory, for more information the reader is referred to Appendix A. This theory has been previously applied by Qin and Librescu [41] and Touraj Farsadi [44] to the thin walled orthotropic beam problem, reducing the 3D problem to a 1D problem. The cross-section is taken into account by calculating its stiffness and mass matrices. Then, the solution is integrated along the beam and the nodal stiffness and mass matrices are obtained.

For each time step, the load estimation submodel is called and generates the aerodynamic load vector as an output. The total aerodynamic load is obtained by adding the quasi-steady forces to the dynamic effects, similarly to Torregrosa et al. [36]. On one hand, the quasi-steady aerodynamic forces are obtained from the CFD polar interpolation, as a function of the angle of attack (α) and plunge (w), see Fig. 4. Then, the coefficients are corrected in an iterative process using the Prandtl Lifting Line Theory [45]. On the other hand, the unsteady effects are estimated at independent sections by means of a Feed Forward Artificial Neural Network (FFN), the reader is referred to Appendix B for the details of the network, using the following inputs: the mean angle of attack ($\bar{\alpha}$), the increment of angle of attack from the mean ($\Delta\alpha$), and its two first derivatives ($\dot{\alpha}$ and $\ddot{\alpha}$). The artificial neural network is the result of the previous work Torregrosa et al. [36]. Therefore, for the sake of brevity the training methodology and test results are not presented in this paper.

Finally, in the coupled solver, the position, velocity and acceleration at the following time step is calculated. The dynamic equation is solved
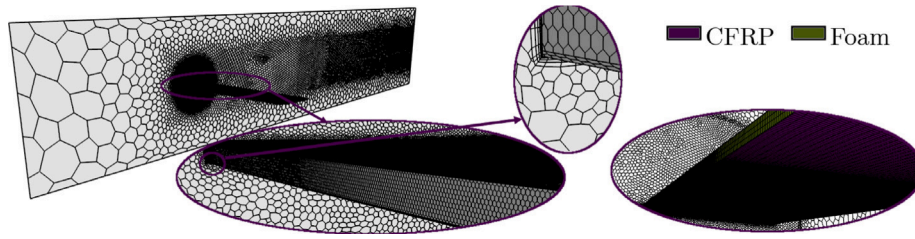
Fig. 2. Mesh of the CSD/CFD simulation, zoom on the wall mesh and the boundary layer. The layup structure is presented, showing the CFRP reinforced foam beam.
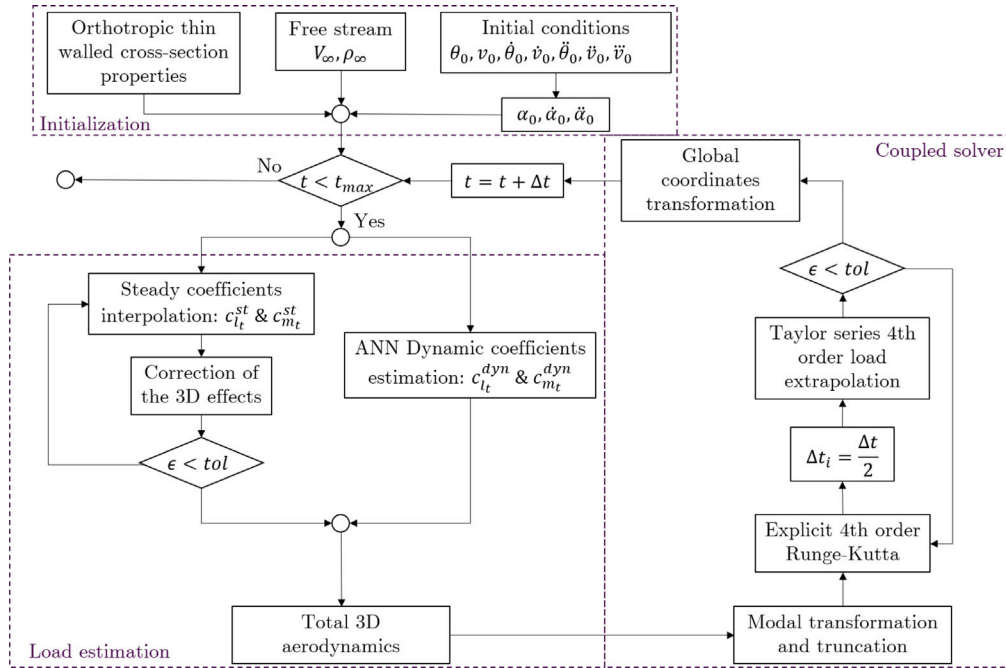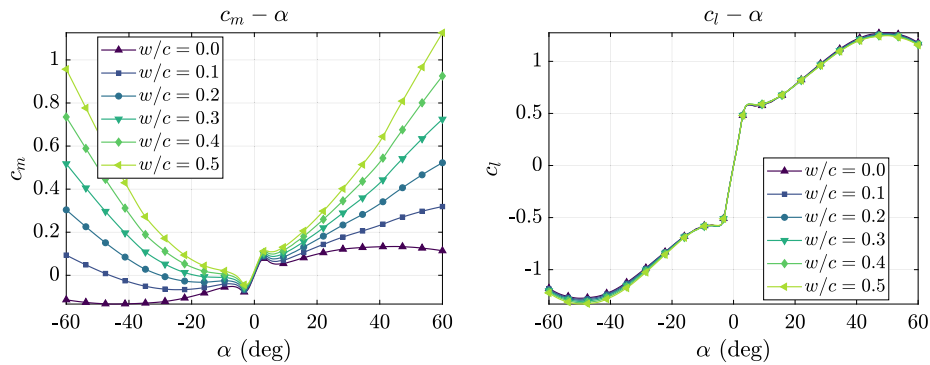

Fig. 3. Scheme of the aeroelastic ROM. The 3D coupled problem is simplified to a 1D beam and the aerodynamic coefficients are solved for a 2D section by means of an ANN and then corrected with 3D effects.

(a) Moment coefficient as a function of the angle of attack and plunge.

(b) Lift coefficient as a function of the angle of attack and plunge.

Fig. 4. Aerodynamic coefficients as a function of the angle of attack and plunge. The coefficients have been obtained from CFD simulations.
Source: Figure taken from Torregrosa et al. [36].

for the n first modes of the beam by applying a modal truncation. Thus, the contribution of the faster modes is neglected. In addition, modal truncation avoids the neural network to extrapolate the solution, as the training process of the neural network has utilized oscillations of the cross-section relative to the first modes. The contribution of the faster frequencies (truncated modes) might exceed the ANN domain, producing unrealistic results.

The equation of the section motion, Eq. (1), is solved using an explicit 4th order Runge–Kutta scheme. In this equation $\mathbf{M}$, $\mathbf{K}$, $\vec{u}$ and $\vec{F}$ represent the mass and stiffness matrices and the displacement and load vectors respectively. To maintain the stability of the calculation, internal iterations are allowed. An adaptive internal time step is implemented to preserve the error of the solution relative to the double of internal time steps. In addition, aerodynamic loads are extrapolated

Table 2
Validation of the structural model. Natural frequency comparison with the literature.

Mode	Shaat [38]	Banerjee [39]	Minguet [40]		Current
			Analytical	Experimental	
1	1.278 Hz	1.280 Hz	1.280 Hz	1.400 Hz	1.285 Hz
2	8.012 Hz	8.020 Hz	8.010 Hz	8.000 Hz	8.053 Hz
3	22.433 Hz	22.441 Hz	22.500 Hz	20.000 Hz	22.544 Hz
4	43.960 Hz	43.927 Hz	44.400 Hz	68.000 Hz	44.045 Hz
5	–	48.431 Hz	48.700 Hz	–	47.748 Hz

from the previous solution in the internal steps.

$$\mathbf{M}\ddot{\vec{u}} + \mathbf{K}\vec{u} = \vec{F} \tag{1}$$

A mesh, time step and number of modes independence analysis was performed to set the ANN-enhanced ROM simulations, resulting in a beam of 16 elements, a time step of $\Delta t = 2 \cdot 10^{-4}$ s and 4 mode shapes. The detailed procedures are included in the Appendix C.

3. Results and discussion

In this section, the results of the article are presented. At first, the models (structural, aerodynamic and aeroelastic) are validated. The computational cost of the ROM is compared against the full CSD/CFD simulation. Then, the capabilities of the reduced order model in the structural optimization process are demonstrated. In this sense, the influence of the fiber orientation is analyzed for different working conditions.

3.1. Structural model validation

As stated in Sections 1, the structural model was validated against the literature before the aeroelastic simulation. The structural validation test was performed by comparing the natural frequencies of a carbon fiber laminated beam taken from Minguet [46] with the results of the current model. In Table 2 the comparison of the natural frequencies is presented, showing good agreement with similar 1D models. Note that the experimental data was obtained with a tip deflection of 137 mm and nonlinear structural effects appeared, which explains the differences in mode 4. The mode shapes of the structure are shown in Fig. 5. Structural coupling is evidenced in all the mode shapes, as the beam is twisting and bending in the same vibration mode. For the first mode both twist and plunge increase with the longitudinal coordinate. This is the dominating mode of the aeroelastic motion. In the second and third modes the torsion presents a zero when the plunge amplitude derivative is null. For the fourth mode the torsion increases along the longitudinal coordinate while the vertical displacement has two relative maxima and two relative minima. The aeroelastic dynamic motion of the beam is expected to reproduce the first mode with small vibrations of the second, third and fourth modes.

3.2. Aerodynamic model results and limitations

Complex nonlinear aerodynamic patterns can be observed from the three dimensional simulations. Near the beam free tip, recirculation couples with tip vortex effects, displacing the pressure center of the sections near the tip and, thus, modifying the moment coefficient with respect to the value estimated with the Lifting Line Theory. In Fig. 6, the aerodynamic effects of the tip vortex are presented. The figure shows the distribution of the pressure coefficient along the span of the beam, evidencing that the nonlinearities of the aerodynamic loads are induced in first term by a recirculation area near the leading edge. The recirculation area is reduced near the tip, where the pressure is homogenized as an effect of the vortex. In the wing span 5 color rectangles indicate the measured cross-sections, for which the pressure coefficient is presented. In the bottom of the figure, the pressure

coefficient distribution of the previously mentioned cross sections are presented following the previous color code. In addition, the direction of the wall shear loads is included in the image. The shear stress lines show the limit of the recirculation area and its reduction in the suction side near the tip. Finally, the center of pressure position moves near the tip vortex (the color points reference the cross sections indicated over the surface.

Although the Lifting Line Theory fails when estimating three-dimensional effects near the tip (due to the movement of the center of pressure), as shown in Fig. 7, the error remains below 4%.

3.3. Aeroelastic validation against CSD/CFD

The solution of the complete CSD/CFD simulation was compared with the results of the ROM in order to determine the accuracy of the procedure. Firstly, the deviation between the ROM and CFD/CSD aeroelastic results was evaluated. Fig. 8, shows the comparison between the mean deformation values of the CSD/CFD simulations and the ROM model. The continuous line represents the perfect agreement between both methodologies. The points below the line in Fig. 8(a) indicate that the ROM tends to underestimate the plunge motion, whereas in Fig. 8(b) they show higher twist in absolute value. According with the figure, the reduced order model is able to obtain results similar to those of the high-cost solution. However, the error increases as the deformations grow.

In Fig. 9 comparison of the evolution of the mean values is shown as a function of the nondimensional carbon fiber stiffness, $E^* = \frac{E_l^c}{\frac{1}{2}\rho_\infty v_\infty^2} \left(\frac{h}{c}\right)^3$. In the figure the effects of the fiber direction can be observed. When the fibers are oriented longitudinally, the elastic modulus of the material is higher in the normal stress direction (where the bending loads act) and, therefore, the bending deformation is lower. In addition, the asymptotic behavior of the system can be appreciated: the air–structure coupling acts reducing the nondimensional stiffness of the structure as the flow velocity increases and thus an asymptotic limit appears for low nondimensional stiffness.

The mean twist is shown in Fig. 10. Both models show good agreement for longitudinal and oblique orientation of the fibers, and similar effects to the plunge can be observed. In addition, as the elastic axis of the structure (without bending–torsion coupling) is coincident with its center of gravity, no dynamic instabilities are expected. The structure should be expected to collapse near the divergence velocity (the asymptotic value of the velocity) where the angle of attack will increase dramatically and the structure will stall and oscillate (stall flutter).

According to the previous figures, plunge and twist are demonstrated to be accurately captured by the Reduced Order Model, indicating that the methodology is capable of predicting the influence of the fiber orientation on the structural design. The Reduced Order Model enhanced by Artificial Neural Networks is evidenced to provide accurate simulations for high nondimensional stiffness. However, a progressive increase in the error near the instability conditions was detected. The values of the asymptote are shifted from the CFD/CSD solution, see Fig. 8. Nevertheless, the accuracy remains sufficiently high so as to predict aeroelastic phenomena such as flutter, divergence or limit cycle oscillations (LCO), and the computational cost of the calculation is decreased by orders of magnitude. Note that the nonlinearities leading to the LCO are provided by the aerodynamic model, as the structure remains linear in the present work.

The computational cost was measured for the different computing tools. The CFD/CSD simulations were performed on a 15 Intel® Xeon® Gold 6154 CPUs multiuser cluster whereas ROM simulations were run on an Intel® Xeon® CPU ES-2630 v2. The CPU computing time required for a time step in the CFD/CSD simulation is slightly above $2 \cdot 10^4$ s and the complete simulation requires 430 h, while for the ROM the CPU time per time step is around 2.2 s and the simulation needs approximately 3 h, what implies a decrease of more than two orders of magnitude and four orders of magnitude in the total simulation and CPU computational cost respectively.
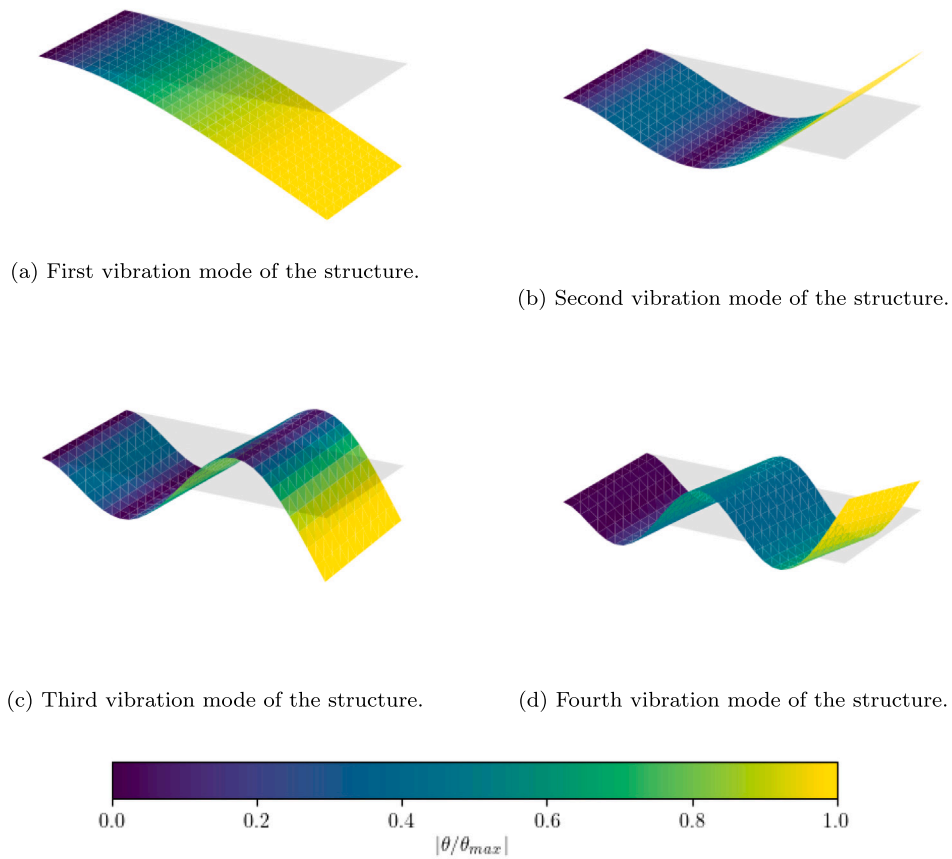
(a) First vibration mode of the structure.

(b) Second vibration mode of the structure.

(c) Third vibration mode of the structure.

(d) Fourth vibration mode of the structure.

$|\theta/\theta_{max}|$

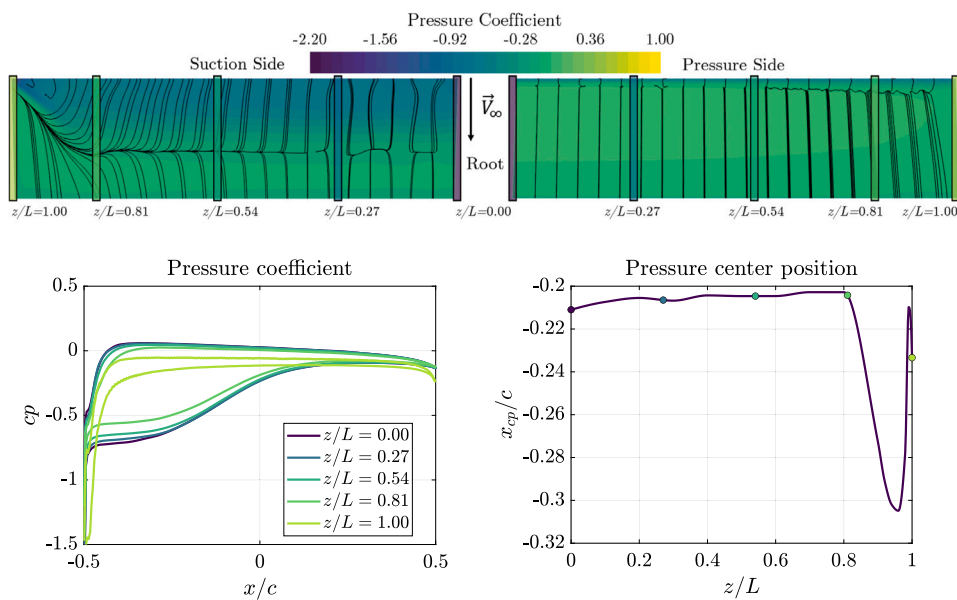**Fig. 5.** Mode shapes (not-scaled) of the beam structure based on Minguet [46].

Fig. 6. Tip vortex effects, pressure distribution and pressure center position over the structure surface.
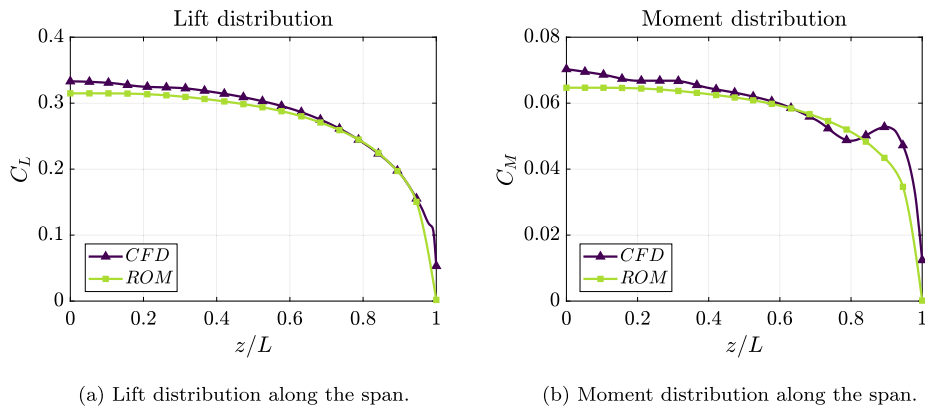
(a) Lift distribution along the span.

(b) Moment distribution along the span.

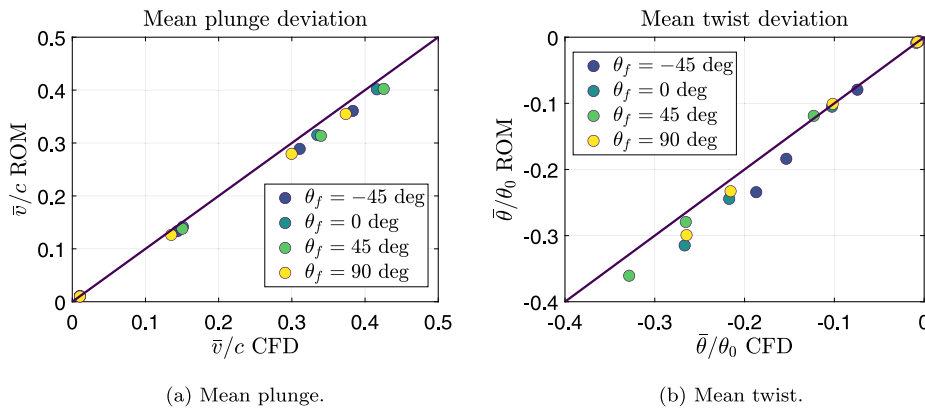**Fig. 7.** Steady aerodynamic load distribution along the span for 3D CFD simulations and 3D ROM analysis.

(a) Mean plunge.

(b) Mean twist.

Fig. 8. Deviation of the ROM solution with respect to CFD/CSD simulations.
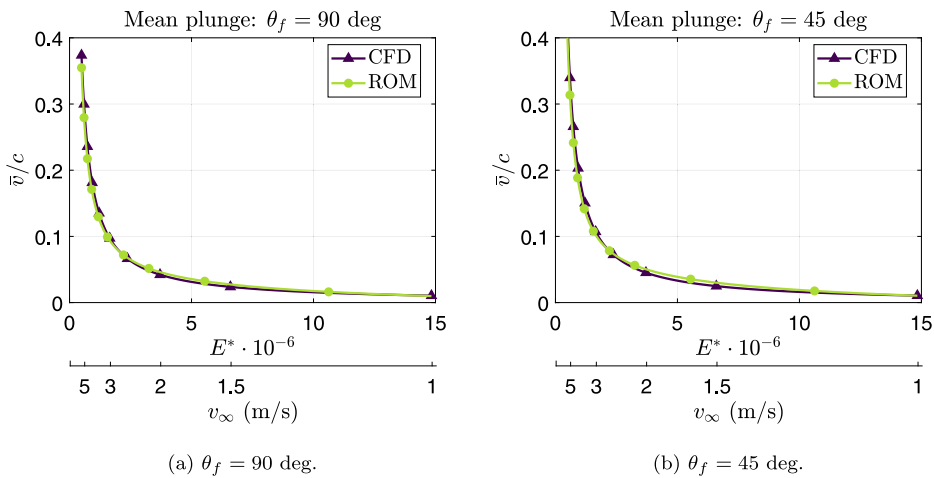

(a) $\theta_f = 90$ deg.

(b) $\theta_f = 45$ deg.

Fig. 9. Plunge evolution of CFD and ROM calculations for different fiber orientations. Note that the velocity measurements correspond to a structure of the properties listed in Table 1.

3.4. Influence of fiber orientation

Fiber orientation influences the aeroelastic behavior of the structure. The ROM was applied to a range of orientations from −90 to 90 deg. Fig. 11 shows the variations of the mean deformation as a function of the nondimensional stiffness and the fiber orientation. A reduction on the mean twist is observed for negative orientations of the fiber. This fact matches the results found in the literature [14], as washout effect is applied to the structure, resulting in an alleviation of the aerodynamic load. In other words, the plunge of the beam generates a reduction on the angle of attack, acting as a passive aeroelastic control. Moreover, as the twist has been reduced, the aerodynamic force is also decreased, resulting in a lower plunge. Inverse effects are obtained for positive orientations, generating higher deformations and resulting in a lower unstable free stream velocity.
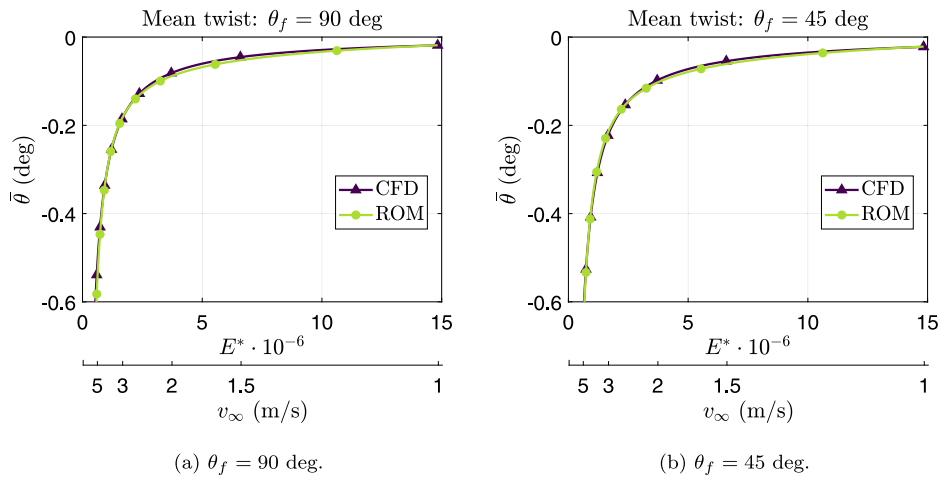
7

(a) $\theta_f = 90$ deg.   (b) $\theta_f = 45$ deg.

Fig. 10. Twist evolution of CFD and ROM calculations for different fiber orientations. Note that the velocity measurements correspond to a structure of the properties listed in Table 1.
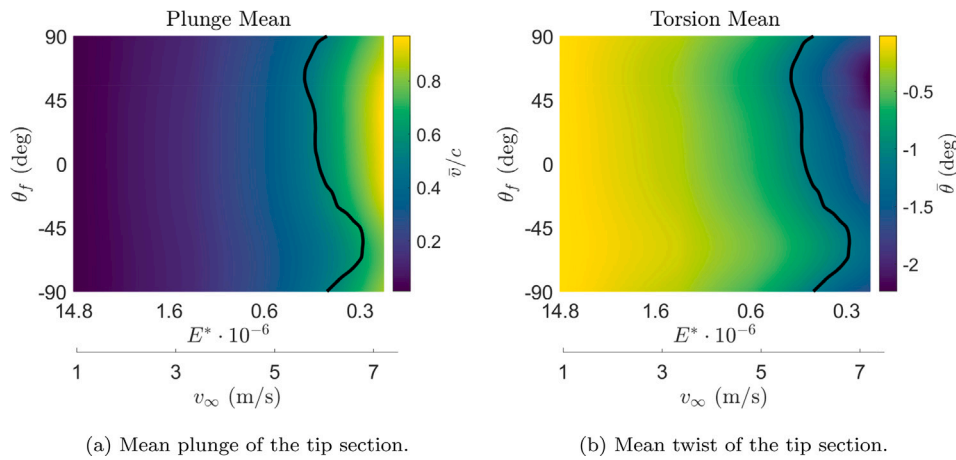

(a) Mean plunge of the tip section.   (b) Mean twist of the tip section.

Fig. 11. Mean deformation of the tip section as a function of the velocity and fiber orientation. The solid line limits the stable region.

Additionally to the structural couplings described in the literature, the current methodology includes the simulation of aerodynamic nonlinear effects, improving the results near the instability with respect to the linear potential aerodynamic model [11].

The stability limit of the system was estimated by the damping of the solution signal and it is presented by the solid line in Figs. 11 and 12. Fig. 12(a) includes the torsion damping of the system. As it can be observed, inside the stable region the aerodynamic damping increases with velocity for negative values of the fiber orientation. This effect is in accordance with the information found in the literature [12,47]. The negative orientation of the fiber (fiber rotated to the leading edge) produces wash-out: the twist of the tip is reduced when its plunge increases. Therefore, the mean torsion is lower than for positive and longitudinal orientations, thus preventing from stall. For a squared-section beam, stall initializes flutter, creating a phenomena known as stall flutter, which is an oscillatory instability dominated by torsion and produced by the aerodynamic nonlinearities. The time evolution of the system for the indicated design points is presented in Fig. 12(b). It shows that the -45 deg orientation remains stable while the rest of configurations are under stall flutter. Therefore, according with Fig. 12(a), for an optimum design the fiber should be in the range $[-44, -68]$ deg for maximizing the stall flutter velocity and protect the structure.

Similar results were obtained for the aerodynamic coefficients. Lift and moment coefficients are shown in Fig. 13. The aerodynamic coefficients are directly related with the angle of attack, in other words, with

the twist of the beam. Thus, the increase in the mean twist generates higher lift and moment coefficients. In addition, the instability appears when the aerodynamic coefficients rise approximately 20% off the rigid beam value. This growth is equivalent to an increment of 1 deg of the mean twist in the tip section. Similar effects were noticed in the drag coefficient. Therefore, the aerodynamic efficiency remains constant for the stability domain. When the instability begins, the coefficients increase, rising the aerodynamic efficiency until the cross-section stalls.

Finally, the modal contribution on the deformed shape is presented in Fig. 14, for the highlighted operational points of Fig. 12. A similar contribution is observed for all the fiber orientations. The displacement of the nodes is mainly affected by the first mode. This means that the phenomenon could be simulated by using an equivalent section. However, as the velocity of the nodes is affected by the first three modes, in case of studying the aeroelastic behavior of the equivalent section the contribution of the velocity of vibration would be omitted.

4. Conclusions

A Reduced Order Model enhanced by Artificial Neural Networks for aeroelastic calculations has been presented. The addition of a Neural Network to the existing Lisbrescu's thin walled beam model has allowed to reproduce nonlinear aerodynamic effects. Thus, nonlinear oscillatory phenomena have been simulated. The model has been tested for a carbon fiber reinforced foam squared-section beam clamped in one of the ends. The methodology of the solver has been described, the solver
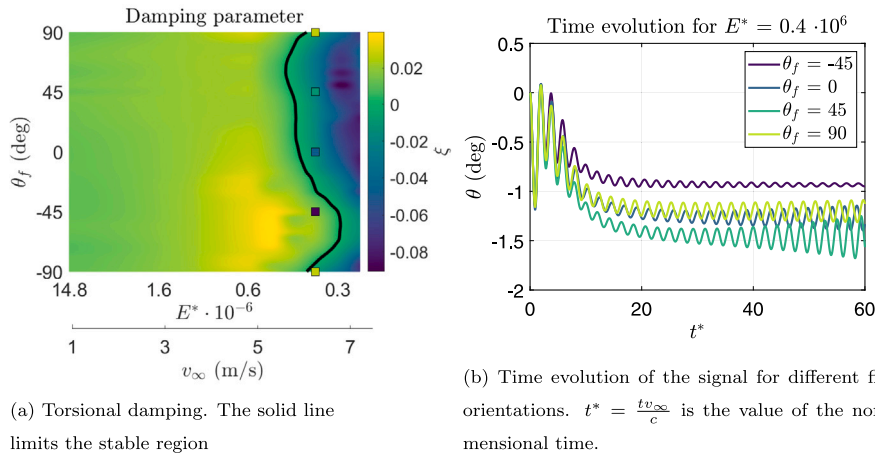
(a) Torsional damping. The solid line limits the stable region

(b) Time evolution of the signal for different fiber orientations. $t^* = \frac{tv_\infty}{c}$ is the value of the nondimensional time.

Fig. 12. Torsional damping and evolution of the torsion of the system for different flow and structural conditions. The time evolution, Fig. 12(b), is shown for the highlighted color squares in the damping map, Fig. 12(a).
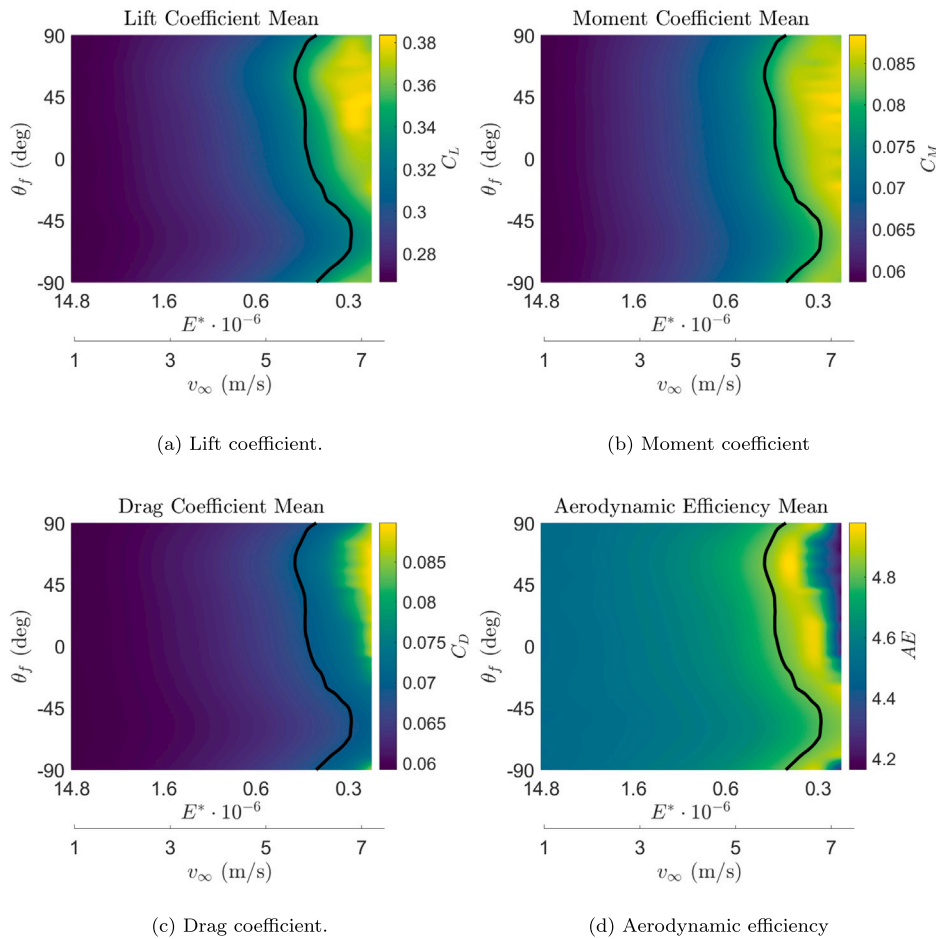

(a) Lift coefficient.

(b) Moment coefficient

(c) Drag coefficient.

(d) Aerodynamic efficiency

Fig. 13. Aerodynamic coefficients of the beam for different flow and structural conditions. The solid lines limit the stable regions.

have been validated against the literature and the results have been compared with high fidelity CSD/CFD simulations. Finally, the behavior of the beam have been analyzed for different fiber orientations, showing the influence of the fiber direction on the solution and the applicability of ROMs in the structural design process.

With respect to the methodology, ROMs have demonstrated to be an efficient low fidelity tool for calculating the aeroelastic behavior of the structure. A reduction of four orders of magnitude of CPU cost has been

noticed in the previous calculations. In addition, the error registered when comparing with complex CSD/CFD simulations remains under 2% far from the instability and increases near the asymptote up to a 15%. However, the increase in the error is not a limitation for the use of the methodology in the ROM, as the nondimensional curves fit for both methodologies. The increase in the error is due to a slight deviation of approximately 5% on the asymptote.
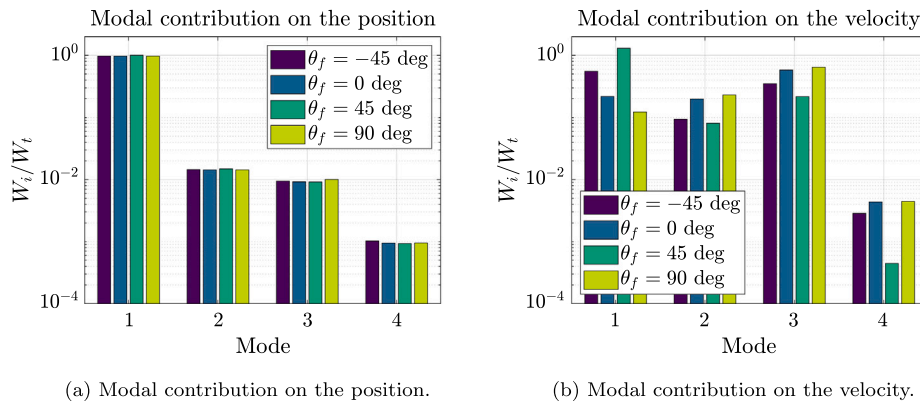
(a) Modal contribution on the position.

(b) Modal contribution on the velocity.

Fig. 14. Squared mean modal contribution of the last 0.2 s of simulation for position and velocity for $E^* = 0.4 \cdot 10^6$.

In addition, the structural optimization capabilities of the model have been tested by simulating a batch of operational points in which the bending–torsion coupling effects have been analyzed. The wash-out effects presented in the literature have demonstrated to prevent from stall flutter. The fibers should be rotated upwash to generate a reduction of the angle of attack when the plunge is increased. For the geometry studied, a range of $[-44, -68]$ deg has been obtained as the more effective in the protection of the structure.

Regarding the modal contribution, the first mode is dominant in the displacement. Differently from the isotropic material, plunge and twist are contained in the same mode. In addition, the second and third modes contribute to the velocity of the sections, and thus to the aerodynamic damping. Therefore, if the problem is reduced to an equivalent section, only the first bending and the first torsion mode are required. In the case of oblique fibers both modes (plunge and twist) are contained in the first vibration mode. Thus, only this mode is necessary for reproducing the behavior of the beam, and the effects of velocity (secondary modes) would be canceled.

As a summary, the benefits and limitations of the ANN enhanced ROM have been analyzed. The methodology has proved to be a powerful tool in the predesign process, allowing to establish an optimum structure and reducing the number of high fidelity simulations required for an optimization process, decreasing computational cost and speeding up the design by orders of magnitude.

CRediT authorship contribution statement

A.J. Torregrosa: Project administration, Writing – review & editing. **A. Gil:** Resources, Writing – review & editing. **P. Quintero:** Conceptualization, Supervision, Writing – review & editing. **A. Cremades:** Conceptualization, Methodology, Software, Validation, Investigation, Writing – original draft, Visualization.

Declaration of competing interest

The authors declare that they have no known competing financial interests or personal relationships that could have appeared to influence the work reported in this paper.

Data availability

The raw/processed data required to reproduce these findings cannot be shared at this time due to technical or time limitations.

Appendix A. Definition of the structural model

In this section, the structural equations are derived from first principles, obtaining the stiffness and mass matrices. This section follows the methodology presented by Librescu and Song [37].

On one side, relative to the cross-section stiffness, the coordinates x and y of the beam element local reference frame are used for describing the cross section, while the z axis is used for the longitudinal coordinate, Fig. A.15(a). The linear displacements in coordinates x, y, z are denoted by u, v, w, and the respective rotation angles are ϕ, ψ, θ. On the other side, the cross-section reference frame is defined with the wall mean fiber path coordinate s and the thickness coordinate n, as shown in Fig. A.15(b).

Assuming that: the longitudinal displacement w is much smaller than the transverse displacements u and v; the normal stress in the thickness direction is negligible $\sigma_{nn} \approx 0$; the section is rigid $\epsilon_{xx} = \epsilon_{yy} = \epsilon_{xy} = 0$; warping is included and shear strains are uniform in the section, then the displacement of a generic point of the section is defined in Eqs. (A.1)–(A.3).

$$u = u_0 - \left(y - n\frac{dx}{ds}\right)\sin(\theta) - \left(x + n\frac{dy}{ds}\right)(1 - \cos(\theta)) \tag{A.1}$$

$$v = v_0 + \left(x + n\frac{dy}{ds}\right)\sin(\theta) - \left(y - n\frac{dx}{ds}\right)(1 - \cos(\theta)) \tag{A.2}$$

$$w = w_0 - \left(x + n\frac{dy}{ds}\right)\psi + \left(y - n\frac{dx}{ds}\right)\phi - \left(F_w(s) + nr_t(s)\right)\theta' \tag{A.3}$$

Here, index 0 indicates the reference point of the section, the first warping function is defined by the function $F_w(s)$ (Eq. (A.4)), and the second warping function is $nr_t(s)$, where r_t is the tangential distance to an arbitrary point of the mean fiber of the wall. Symbol ($'$) represents the derivative with respect to the z coordinate.

$$F_w(s) = \int_0^s \left(r_n(s) - \Psi\right) ds; \ \Psi = \frac{\oint \frac{r_n(s)ds}{h(s)}}{\frac{ds}{h(s)}} \rightarrow \text{if } h(s) = cte \rightarrow \Psi = \frac{2\Omega}{\beta} \tag{A.4}$$

where $h(s)$ is the thickness of the wall, Ω is the closed area of the section (null in the case of open cross-section), β is its perimeter and $r_n(s)$ is the normal distance to an arbitrary point of the mean fiber of the wall.

The strains are defined through the Green–Lagrange tensor, as in Eqs. (A.5)–(A.7).

$$\epsilon_{zz} = \frac{\partial w}{\partial z} + \frac{1}{2}\left[\left(\frac{\partial u}{\partial z}\right)^2 + \left(\frac{\partial v}{\partial z}\right)^2\right] \tag{A.5}$$

$$\gamma_{sz} = \gamma_{xz}\frac{dx}{ds} + \gamma_{yz}\frac{dy}{ds} + \Psi\phi' + 2n\phi' \tag{A.6}$$

$$\gamma_{nz} = \gamma_{xz}\frac{dy}{ds} - \gamma_{yz}\frac{dx}{ds} \tag{A.7}$$

(a) Local reference frame of the beam element.
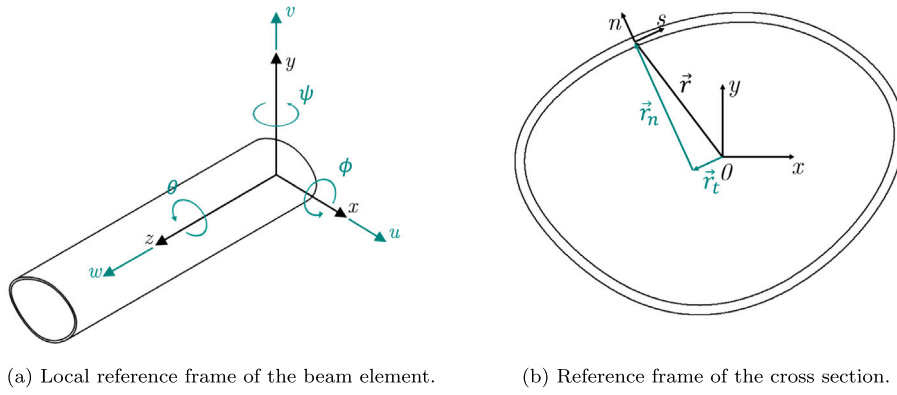

(b) Reference frame of the cross section.

Fig. A.15. Reference frames of the beam element and cross section.

where the tangential strains are defined in global axis by Eqs. (A.8) and (A.9).

$$\gamma_{xz} = -\psi + u'_0 \cos(\theta) + v'_0 \sin(\theta) \tag{A.8}$$

$$\gamma_{yz} = \phi + v'_0 \cos(\theta) - u'_0 \sin(\theta) \tag{A.9}$$

Substituting Eqs. (A.1)–(A.3), (A.8) and (A.9) into Eqs. (A.5)–(A.7) it is possible to obtain an expression of the strains as a function of the n coordinate, as in Eqs. (A.10)–(A.12).

$$\epsilon_{zz} = \epsilon_{zz}^0 + n\epsilon_{zz}^1 + n^2\epsilon_{zz}^2 \tag{A.10}$$

$$\gamma_{sz} = \gamma_{sz}^0 + n\gamma_{sz}^1 \tag{A.11}$$

$$\gamma_{nz} = \gamma_{nz}^0 \tag{A.12}$$

The constitutive equations of the orthotropic ply in the beam and material reference frames (l, t, n) are expressed in Eq. (A.13).

$$\begin{Bmatrix} \sigma_{ss} \\ \sigma_{zz} \\ \tau_{zn} \\ \tau_{sn} \\ \tau_{sz} \end{Bmatrix} = \bar{\mathbf{Q}} \begin{Bmatrix} \epsilon_{ss} \\ \epsilon_{zz} \\ \gamma_{zn} \\ \gamma_{sn} \\ \gamma_{sz} \end{Bmatrix} \rightarrow \begin{Bmatrix} \sigma_{tt} \\ \sigma_{ll} \\ \tau_{ln} \\ \tau_{tn} \\ \tau_{lt} \end{Bmatrix} = \mathbf{Q} \begin{Bmatrix} \epsilon_{tt} \\ \epsilon_{ll} \\ \gamma_{ln} \\ \gamma_{tn} \\ \gamma_{lt} \end{Bmatrix} \tag{A.13}$$

For an orthotropic material, the constitutive matrix $\mathbf{Q}$ in the fiber material reference frame is expressed in Eq. (A.14). In addition, the transformation of the constitutive equations is also included.

$$\mathbf{Q} = \begin{bmatrix} \dfrac{E_t}{1-v_{tl}v_{lt}} & \dfrac{v_{lt}E_t}{1-v_{tl}v_{lt}} & 0 & 0 & 0 \\ \dfrac{v_{lt}E_t}{1-v_{tl}v_{lt}} & \dfrac{E_l}{1-v_{tl}v_{lt}} & 0 & 0 & 0 \\ 0 & 0 & G_{ln} & 0 & 0 \\ 0 & 0 & 0 & G_{tn} & 0 \\ 0 & 0 & 0 & 0 & G_{tl} \end{bmatrix} \rightarrow \bar{\mathbf{Q}} = \mathbf{T}^{-1}\mathbf{Q}\mathbf{R}\mathbf{T}\mathbf{R}^{-1} \tag{A.14}$$

The coordinate transformation of the constitutive matrix is performed using the rotation matrix $\mathbf{T}$ and the transformation matrix from tensor to engineering strains $\mathbf{R}$. Note that θ_f represents the material orientation.

$$\mathbf{T}$$
$$= \begin{bmatrix} \cos^2\theta_f & \sin^2\theta_f & 0 & 0 & 2\sin\theta_f\cos\theta_f \\ \sin^2\theta_f & \cos^2\theta_f & 0 & 0 & -2\sin\theta_f\cos\theta_f \\ 0 & 0 & \cos\theta_f & -\sin\theta_f & 0 \\ 0 & 0 & \sin\theta_f & \cos\theta_f & 0 \\ -\sin\theta_f\cos\theta_f & \sin\theta_f\cos\theta_f & 0 & 0 & \cos^2\theta_f - \sin^2\theta_f \end{bmatrix} \tag{A.15}$$

$$\begin{Bmatrix} \epsilon_{tt} \\ \epsilon_{ll} \\ \gamma_{ln} \\ \gamma_{tn} \\ \gamma_{lt} \end{Bmatrix} = \mathbf{R} \begin{Bmatrix} \epsilon_{ll} \\ \epsilon_{tt} \\ \epsilon_{ln} \\ \epsilon_{tn} \\ \epsilon_{lt} \end{Bmatrix} \rightarrow \mathbf{R} = \begin{bmatrix} 1 & 0 & 0 & 0 & 0 \\ 0 & 1 & 0 & 0 & 0 \\ 0 & 0 & 2 & 0 & 0 \\ 0 & 0 & 0 & 2 & 0 \\ 0 & 0 & 0 & 0 & 2 \end{bmatrix} \tag{A.16}$$

Stresses are integrated along the normal coordinate to obtain the forces and moments acting on the mean fiber of the walls. The membrane forces are shown in Eqs. (A.17), the transverse shear resultants in Eq. (A.18), the stress couples in Eq. (A.19) and the high order stress couple in Eq. (A.20).

$$N_{ss} = \sum_{k=1}^{M} \int_{h_{k-1}}^{h_k} \sigma_{ss} dn; \ N_{zz} = \sum_{k=1}^{M} \int_{h_{k-1}}^{h_k} \sigma_{zz} dn; \ N_{sz} = \sum_{k=1}^{M} \int_{h_{k-1}}^{h_k} \sigma_{sz} dn \tag{A.17}$$

$$N_{zn} = \sum_{k=1}^{M} \int_{h_{k-1}}^{h_k} \sigma_{zn} dn; \ N_{sn} = \sum_{k=1}^{M} \int_{h_{k-1}}^{h_k} \sigma_{sn} dn \tag{A.18}$$

$$L_{zz} = \sum_{k=1}^{M} \int_{h_{k-1}}^{h_k} \sigma_{zz} n \, dn; \ L_{sz} = \sum_{k=1}^{M} \int_{h_{k-1}}^{h_k} \sigma_{sz} n \, dn \tag{A.19}$$

$$\Gamma_{zz} = \sum_{k=1}^{M} \int_{h_{k-1}}^{h_k} \sigma_{zz} n^2 \, dn \tag{A.20}$$

where M is the total number of layers. The stiffness coefficients of the laminate are defined on Eq. (A.21).

$$(A_{ij}, B_{ij}, D_{ij}, F_{ij}, H_{ij}) = \sum_{k=1}^{M} \int_{h_{k-1}}^{h_k} \bar{Q}_{ij}^{(k)}(1, n, n^2, n^3, n^4) dn \tag{A.21}$$

The internal forces and moments of the structure are expressed as a function of the strains, Eq. (A.22), assuming $\epsilon_{ss} = \epsilon_{ss}^0$ and $\gamma_{sn} = \gamma_{sn}^0$

$$\begin{Bmatrix} N_{zz} \\ L_{zz} \\ \Gamma_{zz} \\ N_{sz} \\ L_{sz} \end{Bmatrix} = \begin{bmatrix} A_{22} & B_{22} & D_{22} & A_{26} & B_{26} \\ B_{22} & D_{22} & F_{22} & B_{26} & D_{26} \\ D_{22} & F_{22} & H_{22} & D_{26} & F_{26} \\ A_{26} & B_{26} & D_{26} & A_{66} & B_{66} \\ B_{26} & D_{26} & F_{26} & B_{66} & D_{66} \end{bmatrix} \begin{Bmatrix} \epsilon_{zz}^0 \\ \epsilon_{zz}^1 \\ \epsilon_{zz}^2 \\ \gamma_{sz}^0 \\ \gamma_{sz}^1 \end{Bmatrix} + \begin{bmatrix} A_{12} \\ B_{12} \\ D_{12} \\ A_{16} \\ B_{16} \end{bmatrix} \{\epsilon_{ss}^0\} \tag{A.22}$$

$$\{ N_{ss} \} = \begin{bmatrix} A_{12} \\ B_{12} \\ D_{12} \\ A_{16} \\ B_{16} \end{bmatrix}^T \begin{Bmatrix} \epsilon_{zz}^0 \\ \epsilon_{zz}^1 \\ \epsilon_{zz}^2 \\ \gamma_{sz}^0 \\ \gamma_{sz}^1 \end{Bmatrix} + \mathbf{M}_3 = \begin{bmatrix} A_{11} \end{bmatrix} \{ \epsilon_{ss}^0 \} \tag{A.23}$$

$$N_{zn} = A_{44}\gamma_{zn}^0 + A_{45}\gamma_{sn}^0 \tag{A.24}$$

$$N_{sn} = A_{45}\gamma_{zn}^0 + A_{55}\gamma_{sn}^0 \tag{A.25}$$

Assuming that $N_{ss} = 0$ and solving the system, the reduced stiffness coefficients are obtained, see Eq. (A.26).

$$K_{11} = A_{22} - \frac{A_{12}^2}{A_{11}}; \; K_{13} = \Psi \left(A_{26} - \frac{A_{12}A_{16}}{A_{11}} \right) + 2 \left(B_{26} - \frac{A_{12}B_{16}}{A_{11}} \right)$$
$$K_{14} = B_{22} - \frac{A_{12}B_{12}}{A_{11}}; \; K_{23} = \Psi \left(A_{66} - \frac{A_{16}^2}{A_{11}} \right) + 2 \left(B_{66} - \frac{A_{16}B_{16}}{A_{11}} \right)$$
$$K_{44} = 2 \left(D_{22} - \frac{B_{12}^2}{A_{11}} \right); \; K_{43} = \Psi \left(B_{26} - \frac{B_{12}A_{16}}{A_{11}} \right) + 2 \left(D_{26} - \frac{B_{12}B_{16}}{A_{11}} \right)$$
$$K_{53} = \Psi \left(B_{66} - \frac{B_{16}A_{16}}{A_{11}} \right) + 2 \left(D_{66} - \frac{B_{16}^2}{A_{11}} \right)$$
$$\tag{A.26}$$

The strain energy of the system is calculated in Eq. (A.27).

$$V = \frac{1}{2} \int_0^L \oint_c \sum_{k=1}^M \int_{h(k)} [\sigma_{zz}\epsilon_{zz} + \tau_{sz}\gamma_{sz} + \sigma_{nz}\gamma_{nz}]_k \, dn \, ds \, dz \tag{A.27}$$

and substituting stresses and strains:

$$V = \frac{1}{2} \int_0^L \left[T_z \left(w_0' + \frac{1}{2}u_0'^2 + \frac{1}{2}v_0'^2 \right) + Q_y \left(\phi + v_0' \cos\theta - u_0' \sin\theta \right) + \right.$$
$$Q_x \left(-\psi + u_0' \cos\theta + v_0' \sin\theta \right) + M_y \left(-\psi' - u_0'\theta' \sin\theta + v_0'\theta' \cos\theta \right) +$$
$$\left. M_x \left(\phi' - u_0'\theta' \cos\theta - v_0'\theta' \sin\theta \right) + M_z\theta' - B_w\theta'' + \frac{1}{2}\Lambda_z\theta'^2 \right] \tag{A.28}$$

Now, the section loads are defined in Eqs. (A.29)–(A.32).

$$T_z = \oint_c N_{zz} \, ds; \; Q_x = \oint_c \left(N_{sz}\frac{dx}{ds} + N_{zn}\frac{dy}{ds} \right) ds \tag{A.29}$$

$$Q_y = \oint_c \left(N_{sz}\frac{dy}{ds} - N_{zn}\frac{dx}{ds} \right) ds; \; M_y = \oint_c \left(-xN_{zz} - L_{zz}\frac{dy}{ds} \right) ds \tag{A.30}$$

$$M_x = \oint_c \left(yN_{zz} - L_{zz}\frac{dx}{ds} \right) ds; \; M_z = \oint_c \left(N_{sz}\Psi + 2L_{sz} \right) ds \tag{A.31}$$

$$B_w = \oint_c \left(N_{zz}F_w(s) + r_t(s)L_{zz} \right) ds;$$
$$\Lambda_z = \oint_c \left(N_{zz} \left(x^2 + y^2 \right) + 2L_{zz}r_n(s) + \Gamma_{zz} \right) ds \tag{A.32}$$

The equations are linearized and the strain energy can be calculated as in Eq. (A.33).

$$V = \frac{1}{2} \int_0^L \vec{D}^T \mathbf{A} \vec{D} \, dz \tag{A.33}$$

where vector $\vec{D}$ is defined in Eq. (A.34) and $\mathbf{A}$ is the stiffness matrix of a cross-section.

$$\vec{D} = \{ w_0' \quad -u_0'' \quad -v_0'' \quad \theta' \quad -\theta'' \}^T \tag{A.34}$$

A similar procedure is developed to calculate the kinetic energy and the mass matrix. The kinetic energy is calculated from Eq. (A.35).

$$K_E = \frac{1}{2} \int_0^L \dot{\vec{U}}^T \mathbf{M} \dot{\vec{U}} \, dz \tag{A.35}$$

Here, $\vec{U} = \{ u_0 \quad v_0 \quad w_0 \quad v_0' \quad u_0' \quad \theta \quad \theta' \}^T$ and $\mathbf{M}$ is the section mass matrix.

On the other hand, relative to the beam model, the stiffness matrix of the beam element is obtained from the integration of matrices $\mathbf{A}$ and $\mathbf{M}$ along the longitudinal coordinate of each element. Finally, the element local matrices are assembled and the global matrix stiffness and mass matrices are calculated.

Appendix B. Artificial neural network training procedure

In this appendix, the architecture of the neural network is presented, the training process is described and the selection criteria for the numbers of neurons and training epochs are shown. The neural network used in this paper has been taken from [36], and therefore the figures included in this appendix were included in the reference work.

Relative to the network architecture, the present ANN uses a feed forward (FFN) architecture, which only needs the current time information to predict the aerodynamics. This architecture allows to reduce the computing cost of the simulation compared to deep-learning neural networks without any important accuracy penalties. The neurons are configured with continuous activation functions to predict continuous coefficients.

ANN reproduce a function as a result of a training process in which the weights and biases need to be fitted. Although any aerodynamic data may be used to train the model, in this work, a set of CFD simulations was used for the training process (90% for training and 10% for validation).

B.1. Neuron independence analysis

The number of neurons used to calculate the aerodynamic model sets the number of weights and variables necessary to adjust the ANN. Therefore, it determines the accuracy and computing cost of training the network [48], but also the probability of network overfitting. The analysis is performed to increase the efficiency of the calculations in terms of computational cost. All the studied ANN are composed by an input layer, a hidden layer with N_1 neurons and an output layer with $N_2 = 2$ neurons. The energetic error of the aerodynamic cycle, ϵE_{c_m}, is calculated to validate the independence analysis. This error is computed as the difference of power coefficients ($c_p = c_m\frac{\dot{\theta}c}{V_\infty}$) integrated in time for CFD and ANN, as stated by Eq. (B.1).

$$\epsilon E_{c_m} = \frac{\int_t^{t+T}(c_{p_{ANN}})dt - \int_t^{t+T}(c_{p_{CFD}})dt}{\int_t^{t+T}(c_{p_{CFD}})dt} \tag{B.1}$$

In Fig. B.16, the power coefficient comparison between CFD and ANN is presented for a network of 2 and 50 neurons (Figs. B.16(a) and B.16(b) respectively). In the figure, an improvement of accuracy compared with the steady solution is observed.

In Fig. B.17 the cycle energetic error density function is shown as a function of the number of neurons of the first layer. The optimum is reached for $N_1 = 50$ when the energetic error becomes constant.

B.2. Optimum number of epochs

In addition, the mean squared error of the training is monitored in order to determine the optimum number of epochs. For the network used, the number of epochs must be set to $5 \cdot 10^3$ to ensure that the error has reached an asymptotic limit or has started to increase. In Fig. B.18, the validation error flattens for $5 \cdot 10^3$ epochs.

B.3. Training results and validation

The dynamic aerodynamic coefficient calculated by means of the neural networks must be added to a stationary aerodynamic coefficient, called quasi-steady model. This quasi-steady model interpolates the coefficients from the steady CFD results, as shown in Fig. 4. Three models are shown in this section: CFD (2D aeroelastic CFD simulations), quasi-steady (aerodynamic coefficients interpolated from steady polar) and FNN (dynamic coefficients calculated by means of FNN added to the quasi-steady coefficient)

In Fig. B.19 the performance of the ANN is shown for training and validation data. The network shows an accurate behavior in the simulation of nonlinear aerodynamics when compared to the quasi-steady approach.
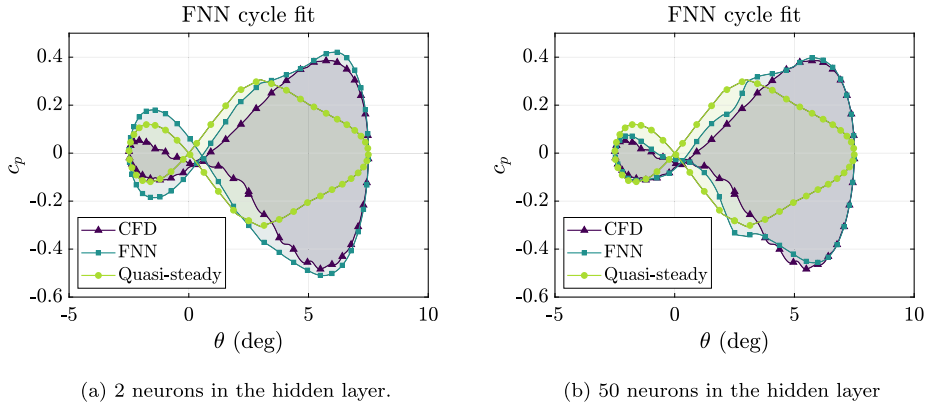
(a) 2 neurons in the hidden layer.   (b) 50 neurons in the hidden layer

Fig. B.16. Power coefficient comparison between the ANNs and the CFD simulations for two representative number of neurons on the hidden layer. The cycle is shown for an initial incidence of 2.5 deg, an amplitude of 5 deg and a nondimensional frequency of $\frac{fc}{V_\infty} = 0.1250$.

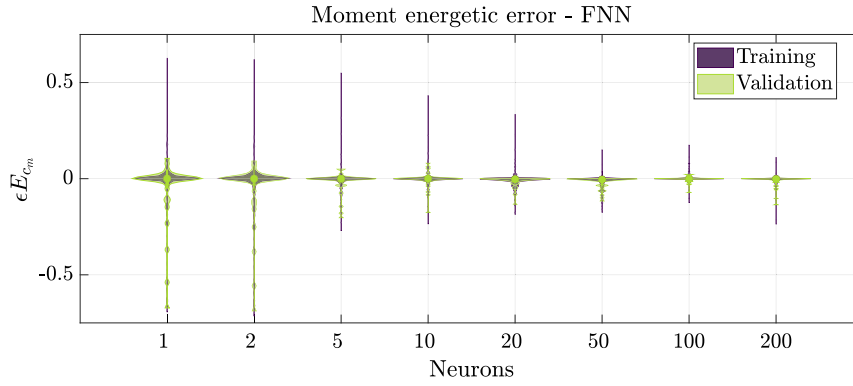*Source:* Figure taken from Torregrosa et al. [36].

Fig. B.17. Distribution of the energy error for the different number of neurons.
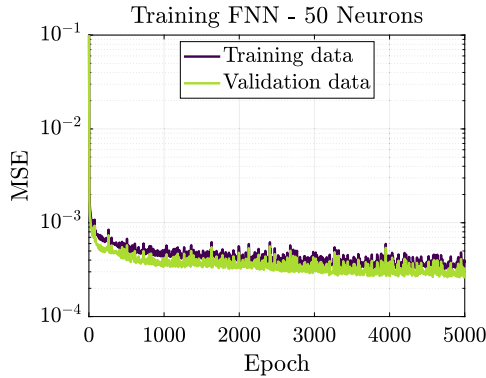*Source:* Figure taken from Torregrosa et al. [36].

Fig. B.18. Evolution of the MSE as a function of the epoch of training for FNN and LSTM networks.
Source: Figure taken from Torregrosa et al. [36].

Appendix C. ROM mathematical description

In this appendix a mathematical description of the algorithms used to solve the coupling between the aerodynamic and structural models is provided.

Firstly, the linear mode analysis of the structure is calculated, obtaining its eigenvalues and eigenvectors. For this purpose, the dynamic equation is normalized, Eq. (C.1).

$$\mathbf{M}\ddot{\vec{u}} + \mathbf{K}\vec{u} = \vec{F} \rightarrow \mathbf{M}^{-1/2}\mathbf{M}\mathbf{M}^{-1/2}\ddot{\vec{q}} + \mathbf{M}^{-1/2}\mathbf{K}\mathbf{M}^{-1/2}\vec{q} = \mathbf{M}^{-1/2}\vec{F} \quad (\text{C.1})$$

where $\vec{u} = \mathbf{M}^{-1/2}\vec{q}$. Then, the mode shapes (eigenvectors) are sorted by the vibration frequency. The final deformation of the beam, $\vec{u}$, can be expressed in terms of the n first modal weights $\vec{y}$, Eq. (C.2).

$$\boldsymbol{\Psi}^T\mathbf{M}^{-1/2}\mathbf{M}\mathbf{M}^{-1/2}\boldsymbol{\Psi}\ddot{\vec{y}} + \boldsymbol{\Psi}^T\mathbf{M}^{-1/2}\mathbf{K}\mathbf{M}^{-1/2}\boldsymbol{\Psi}\vec{y} = \boldsymbol{\Psi}^T\mathbf{M}^{-1/2}\vec{F} \quad (\text{C.2})$$

Here, $\boldsymbol{\Psi}$ is the modal matrix that converts the normalized nodal coordinates $\vec{q}$ to the n first modal weights $\vec{y}$. Eq. (C.2) is redefined to simplify the expression, assuming the relationships shown in Eqs. (C.3)–(C.5).

$$\bar{\mathbf{M}} = \boldsymbol{\Psi}^T\mathbf{M}^{-1/2}\mathbf{M}\mathbf{M}^{-1/2}\boldsymbol{\Psi} \quad (\text{C.3})$$

$$\bar{\mathbf{K}} = \boldsymbol{\Psi}^T\mathbf{M}^{-1/2}\mathbf{K}\mathbf{M}^{-1/2}\boldsymbol{\Psi} \quad (\text{C.4})$$

$$\vec{F}_m = \boldsymbol{\Psi}^T\mathbf{M}^{-1/2}\vec{F} \quad (\text{C.5})$$

Thus, the motion of the structure is expressed by Eq. (C.6).

$$\bar{\mathbf{M}}\ddot{\vec{y}} + \bar{\mathbf{K}}\vec{y} = \vec{F}_m \quad (\text{C.6})$$

The dynamic equation is solved by using an adaptive 4th order Runge–Kutta algorithm. The second order ordinary derivative equation is reduced to first order by creating matrix $\mathbf{A}$ and vector $\vec{b}$. The new state of the system is described by vector $\vec{x}_t$. This algorithm uses Eqs. (C.7) and (C.8) for obtaining the displacements at the next time step.

$$\begin{aligned} \vec{f}_1 &= \mathbf{A}\vec{x}_t + \vec{b} & \vec{f}_2 &= \mathbf{A}\left(\vec{x}_t + \tfrac{1}{2}\vec{f}_1\Delta t_i\right) + \vec{b} \\ \vec{f}_3 &= \mathbf{A}\left(\vec{x}_t + \tfrac{1}{2}\vec{f}_2\Delta t_i\right) + \vec{b} & \vec{f}_4 &= \mathbf{A}\left(\vec{x}_t + \vec{f}_3\Delta t_i\right) + \vec{b} \end{aligned} \quad (\text{C.7})$$

$$\vec{x}_{t+1} = \vec{x}_t + \frac{1}{6}\left(\vec{f}_1 + 2\vec{f}_2 + 2\vec{f}_3 + \vec{f}_4\right)\Delta t_i \quad (\text{C.8})$$
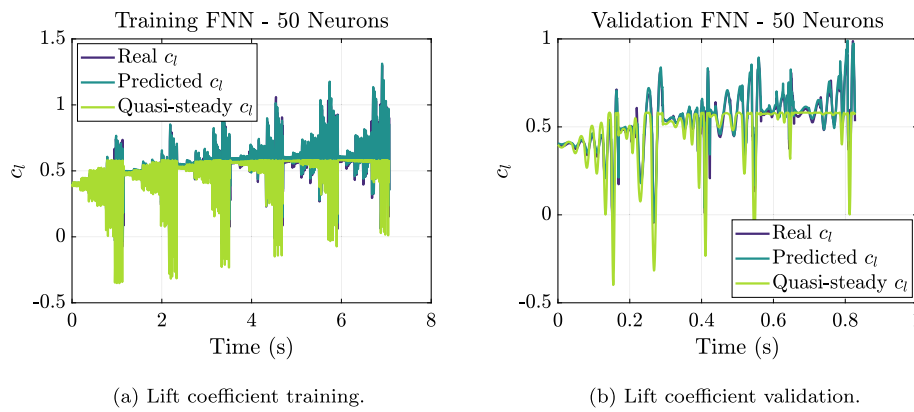
(a) Lift coefficient training.

(b) Lift coefficient validation.

Fig. B.19. Training and validation of the FNN neural network.
Source: Figure taken from Torregrosa et al. [36].

In order to stabilize the results of this solver, the value of Δt_i is iterated for each time step to ensure the convergence of the problem, as explicit solvers may diverge if its value exceeds the stability limit.

The aerodynamic forces are calculated only in the initial value of time step Δt and updated through Taylor series, Eq. (C.9), in the internal iterations.

$$d_{i,0} = f_i; \quad d_{i,1} = \frac{f_i - f_{i-1}}{\Delta t_i}; \quad d_{i,2} = \frac{d_{i,1} - d_{i-1,1}}{\Delta t_i};$$

$$d_{i,3} = \frac{d_{i,2} - d_{i-1,2}}{\Delta t_i}; \quad d_{i,4} = \frac{d_{i,3} - d_{i-1,3}}{\Delta t_i}; \quad f_{i+1} = \sum_{j=0}^{4} \frac{d_{i,j} \left(\Delta t_i\right)^j}{j!} \qquad (C.9)$$

References

[1] Shaw AD, Dayyani I, Friswell MI. Optimisation of composite corrugated skins for buckling in morphing aircraft. Compos Struct 2015;119:227–37.

[2] Sabiston T, Kang BL, Wilkinson D, Engler-Pinto C. Accounting for the microstructure in the prediction of the fatigue lifeof injection moulded composites for automotive applications. Compos Struct 2021;255:112898.

[3] Gargano A, Pingkarawat K, Blacklock M, Pickerd V, Mouritz AP. Comparative assessment of the explosive blast performance of carbonand glass fibre-polymer composites used in naval ship structures. Compos Struct 2017;171:306–16.

[4] Rafiee R, Tahani M, Moradi M. Simulation of aeroelastic behavior in a composite wind turbine blade. J Wind Eng Ind Aerodyn 2016;151:60–9.

[5] Wang L, Quant R, Kolios A. Fluid structure interaction modelling of horizontal-axis wind turbine blades based on CFD and FEA. J Wind Eng Ind Aerodyn 2016;158:11–25.

[6] Pascual Agullo C. Translucent load-bearing GFRP envelopes for daylighting and solar cell integration in buliding construction [Ph.D. thesis], Laussane: EPFL; 2014.

[7] Pascual C, de Castro J, Schueler A, Keller T. Integration of dye solar cells in load-bearing translucent glass fiber-reinforced polymer laminates. J Compos Mater 2016;51:939–53.

[8] Krein A, Williams G. Flightpath 2050: Europe's vision for aeronautics. In: Innovation for sustainable aviation in a global environment, proceedings of the sixth european aeronautics days, Madrid. 2012. p. 63.

[9] Khalil YF. Eco-efficient lightweight carbon-fiber reinforced polymer for environmentally greener commercial aviation industry. Sustain Prod Consum 2017;12:16–26.

[10] Rajpal D, Gillebaart E, Breuker RD. Preliminary aeroelastic design of composite wings subjected to critical gust loads. Compos Struct 2019;85:96–112.

[11] Attaran A, Majid DL, Basri S, Mohd Rafie AS, Abdullah EJ. Structural optimization of an aeroelastically tailored composite flat plate made of woven fiberglass/epoxy. Aerosp Sci Technol 2011;15:393–401.

[12] Chadra R, Stemple AD, Chopra I. Thin-walled composite beams under bending, torsional, and extensional loads. J Aircr 1990;184:872–82.

[13] Geroghiades GA, Banerjee JR. Flutter modes of composite wings exhibiting wash-in and wash-out. In: 38th structures, structural dynamics and materials conference. 1997.

[14] Stanford BK, Jutte CV, Wu KC. Aeroelastic benefits of tow steering for composite plates. Compos Struct 2014;118:416–22.

[15] Meng M, Le HR, Rizvi MJ, Grove SM. 3D FEA modelling of laminated composites in bending and their failuremechanisms. Compos Struct 2015;119:693–708.

[16] Kaviani HR, Nejat A. Investigating the aeroelasticity effects on aeroacoustics and aerodynamics of a MW-class HAWT. J Wind Eng Ind Aerodyn 2021;213:104617.

[17] Dai L, Zhou Q, Zhang Y, Yao S, Kang S, Wang X. Analysis of wind turbine blades aeroelastic performance under yaw conditions. J Wind Eng Ind Aerodyn 2017;171:273–87.

[18] Feil R, Pflumm T, Bortolotti P, Morandini M. A cross-sectional aeroelastic analysis and structural optimization tool for slender composite strictures. Compos Struct 2020;253:112755.

[19] Dowell E. A modern course in aeroelasticity. Springer; 2015.

[20] Baxevanou CA, Chaviaropoulos PK, Voutsinas SG, Vlachos NS. Evaluation study of a Navier-Stokes CFD aeroelastic model of wind turbine airfoils in classical flutter. J Wind Eng Ind Aerodyn 2008;96:1425–43.

[21] Gil A, Tiseira A, Quintero P, Cremades A. Prediction of the non-linear aeroelastic behavior of a cantilever flat plate and equivalent 2D model. Aerosp Sci Technol 2021;113:106685.

[22] Ghafari E, Rezaeepazhand J. Two dimensional cross-sectional analysis of composite beams using Rayleigh-Ritz-based dimensional reduction method. Compos Struct 2018.

[23] Carrera E, Filippi M, Zappino E. Free vibration analysis of rotating composite blades via carrera unified formulation. Compos Struct 2013;106:317–25.

[24] Dhadwal MK, Jung SN. On boundary effects due to nonuniform shear and torsional warping for open section anisotropic beams. Compos Struct 2017;161:350–61.

[25] Farsadi T, Asadi D, Kurtaran H. Flutter improvement of a thin walled wing engine system by applying curvilinear fiber path. Aerosp Sci Technol 2019;93:105353.

[26] Librescu L, Thangjitham S. Analytical studies on static aeroelastic behavior of forward-swept composite wing structures. J Aircr 1991;28:151–7.

[27] Dongmei H, Shiqing H, Xuhui H, Xue Z. Prediction of wind loads on high-rise building using a BP neural network combined with POD. Aerosp Sci Technol 2017;170:1–17.

[28] Ma K, Hu C, Zhou Z. Investigation on vortex-induced vibration of twin rectangular 5:1 cylinders through wind tunnel tests and POD analysis. J Wind Eng Ind Aerodyn 2019;187:97–107.

[29] Tan ZX, Xu YL, Zhu LD, Zhu Q. POD-based modelling of distributed aerodynamic and aeroelastic pressures on bridge decks. J Wind Eng Ind Aerodyn 2018;179:524–40.

[30] Li D, Ronch AD, chen G, Li Y. Aeroelastic global structural optimization using an efficient CFD-based reduced order model. Aerosp Sci Technol 2019;94:105354.

[31] Castellon DF, Fenerci A, Oiseth O. A comparative study of wind-induced dynamic response models of long-span bridges using artificial neural networks, support vector regressionand buffeting theory. J Wind Eng Ind Aerodyn 2021;209:104484.

[32] Wu T, Kareem A. Modeling hysteretic nonlinear behavior of bridge aerodynamics via cellular automata nested neural network. J Wind Eng Ind Aerodyn 2011;99:378–88.

[33] Chen C-H, Wu J-C, Chen J-H. Prediction of flutter derivatives by artificial neural networks. J Wind Eng Ind Aerodyn 2008;96:1926–37.

[34] Abbas T, Kavrakov I, Morgenthal G, Lahmer T. Prediction of aeroelastic response of bridge decks using artificial neural networks. Comput Struct 2020;231:106198.

[35] Li T, Wu T, Liu Z. Nonlinear unsteady bridge aerodynamics: Reduced-order modeling based on deep LSTM networks. J Wind Eng Ind Aerodyn 2020;198:104116.

[36] Torregrosa AJ, García-Cuevas LM, Quintero P, Cremades A. On the application of artificial neural network for the development of a nonlinear aeroelastic model. Aerosp Sci Technol 2021;115:106845.

[37] Librescu L, Song O. Thin-walled composite beams. Theory and application. Springer; 2006.

[38] Shaat M, Aidi B, Case SW, Abdelkefi A. Predictions of the frequencies of bending-torsion coupled laminated composite plates with discontinuities: Novel analytical modeling and experimental validation. Compos Struct 2017;180:334–50.

[39] Banerjee JR. Explicit analytical expressions for frequency equation and mode shapes of composite beams. Int J Solids Struct 2001;38:2415–26.

[40] Minguet P, Dugundji J. Experiments and analysis for composite blades under large deflections part II: Dynamic behavior. AIAA J 1990;1580–8.

[41] Qin Z, Librescu L. Static/Dynamic solutions and validation of a refined anisotropic thin-walled beam model. In: 43rd AIAA/ASME/ASCE/AHS/ASC structures, structural dynamics and materials conference. 2002.

[42] Koohi R, Shahverdi H, Haddadpour H. Nonlinear aeroelastic analysis of a composite wing by finite element method. Compos Struct 2014;113:118–26.

[43] Torregrosa A, Gil A, Quintero P, Ammirati A, Denayer H, Desmet W. Prediction of flow induced vibration of a flat plate located after a bluff wall mounted obstacle. J Wind Eng Ind Aerodyn 2019;190:23–39.

[44] Touraj Farsadi AK. Free vibration analysis of uniform and asymmetric composite pretwisted rotating thin walled beam. In: Proceedings of the international mechanical engineering congress and exposition, advances in aerospace technology, vol. IMECE2017-70531, 2017, p. 3–9.

[45] Anderson Jr JD. Fundamentals of aerodynamics. McGraw-Hill; 1991, p. 324–51.

[46] Minguet PJA. Static and dynamic behavior of composite helicopter rotor blades under large deflections [Ph.D. thesis], Department of Aeronautics and Astronautics, Massachusetts Institute of Technology; 1989.

[47] Chandra R, Chopra I. Experimental-theoretical investigation of the vibration characteristics of rotating composite box beams. J Aircr 1992;29(4).

[48] Kröse B, van der Smagt P. An introduction to neural networks. University of Amsterdam; 1996.